

<https://doi.org/10.1038/s41535-024-00664-0>

Observation of the sliding phason mode of the incommensurate magnetic texture in Fe/Ir(111)

Check for updates

Hung-Hsiang Yang¹, Louise Desplat^{2,3}, Volodymyr P. Kravchuk^{4,5,6}, Marie Hervé⁷, Timofey Balashov⁸, Simon Gerber¹, Markus Garst⁹, Bertrand Dupé^{3,10} & Wulf Wulfhekel^{1,9}✉

The nanoscopic magnetic texture forming in a monolayer of iron on the (111) surface of iridium, Fe/Ir(111), is spatially modulated and uniaxially incommensurate with respect to the crystallographic periodicities. As a consequence, a low-energy magnetic excitation is expected that corresponds to the sliding of the texture along the incommensurate direction, i.e., a phason mode, which we explicitly confirm with atomistic spin simulations. Using scanning tunneling microscopy (STM), we succeed to observe this phason mode experimentally. It can be excited by the STM tip, which leads to a random telegraph noise in the tunneling current that we attribute to the presence of two minima in the phason potential due to the presence of disorder in our sample. This provides the prospect of a floating phase in cleaner samples and, potentially, a commensurate-incommensurate transition as a function of external control parameters.

Incommensurate structures arise when two distinct periodic subsystems coexist but interact only weakly. In this case, their periodicities are, generically, not simply related; the ratio of their wavelength is an irrational number¹. Typical examples are periodic layers of atoms adsorbed on a crystalline substrate², spin- and charge density waves in solids³ or intergrowth compounds⁴. As a characteristic feature, incommensurate structures possess a gapless phason mode representing the sliding of the two periodic subsystems with respect to each other⁵. This phason mode profoundly affects the system's properties: it stabilizes incommensurate structures giving rise to floating phases⁶, it governs, in particular, the optical response of charge-density waves⁷, it causes strong-coupling superconductivity in bismuth at high pressures⁸, and its properties are intimately connected, as shown recently, to the twist-angle variance in twisted bilayer graphene⁹. However, if the interaction between the two subsystems increases, an incommensurate-commensurate (IC-C) transition takes place, where the periodicities become commensurate with the ratio of the respective wavelengths being a rational number. As a consequence, the sliding phason mode acquires an energy gap¹⁰.

Spatially modulated magnetic textures are a prime example for incommensurate phases as discussed early by Dzyaloshinskii¹¹. At the focus of this work is the two-dimensional magnetic texture

materializing in Fe/Ir(111), i.e., in a monolayer of iron on the (111) surface of iridium, that was discovered and characterized in the seminal works of von Bergmann et al.¹² and Heinze et al.¹³. Iron forms a two-dimensional hexagonal lattice on Ir(111) with lattice constant $a = 2.715 \text{ \AA}$, whereas the magnetic texture is an approximate square lattice with lattice constant $A \approx 1 \text{ nm}$. It was shown in ref. 13 that the strong Dzyaloshinskii-Moriya interaction at the Fe/Ir(111) interface and the four-spin interaction play a central role in stabilizing the magnetic modulation with a relatively small periodicity of only $A/a \approx 3.68$. The magnetic texture is thus nanoscopic¹³ and far from the continuum limit as the rotation of spins from lattice site to lattice site is on the order of $360^\circ a/A \approx 100^\circ$.

A system composed of two-dimensional hexagonal and square lattices, representing the arrangement of iron and the magnetic texture of Fe/Ir(111), respectively, is especially interesting because the two distinct symmetries preclude a complete commensurability. A previous example known to us is the adsorption of Argon on the (100) surface of MgO^{2,14}. Whereas the MgO substrate has square lattice symmetry the lateral interaction between adsorbed Ar favors an incommensurate hexagonal arrangement at high Ar densities. If the Ar density is reduced, two subsequent uniaxial IC-C transitions take place, where a commensurability is first attained along one $\langle 100 \rangle$

¹Physikalisches Institut, Karlsruhe Institute of Technology, Wolfgang-Gaede Strasse 1, Karlsruhe, Germany. ²Université de Strasbourg, CNRS, Institut de Physique et Chimie des Matériaux de Strasbourg, UMR 7054, Strasbourg, France. ³Nanomat/Q-mat/CESAM, Université de Liège, Sart Tilman, Belgium. ⁴Institut für Theoretische Festkörperphysik, Karlsruhe Institute of Technology, Karlsruhe, Germany. ⁵Leibniz-Institut für Festkörper- und Werkstofforschung, IFW Dresden, Dresden, Germany. ⁶Bogolyubov Institute for Theoretical Physics of the National Academy of Sciences of Ukraine, Kyiv, Ukraine. ⁷Institut des NanoSciences de Paris, Sorbonne University and CNRS-UMR7588, 4 place Jussieu, Paris, France. ⁸II. Physikalisches Institut B, RWTH Aachen University, Otto-Blumenthal Strasse, Aachen, Germany. ⁹Institute for Quantum Materials and Technology, Karlsruhe Institute of Technology, Karlsruhe, Germany. ¹⁰Fonds de la Recherche Scientifique (FNRS), Bruxelles, Belgium. ✉e-mail: wulf.wulfhekel@kit.edu

axis and afterwards along the other axis, thereby changing the lattice symmetry from hexagonal to orthorhombic.

Similarly, it seems that the symmetry of the magnetic texture in Fe/Ir(111) also deviates from that of a square lattice to enhance commensurability. Its periodicity is, except at zero magnetic field, well resolved by spin-polarized scanning tunneling microscopy (STM)¹² indicating that the texture is not floating on the time scale of the STM experiment. It was pointed out in ref. 12 that a fully commensurate 3 × 5 magnetic texture closely resembles the observations by STM implying a distortion from a square to a centered rectangular lattice with $A/a = \sqrt{13} \approx 3.61$, see Fig. 1a. However, a careful analysis of second-order magnetic Bragg peaks obtained via scans of the tunneling anisotropic magnetoresistance (TAMR) suggested a small deviation from this commensurability¹³. This poses the question whether the magnetic texture is fully incommensurate or discrete domains are formed by pinning and whether different phases exist that are separated by uniaxial IC-C transitions, that can be controlled by temperature, magnetic field, or another parameter.

In order to shed light on these questions, we investigate in the present work the properties of the sliding phason mode expected for an incommensurate magnetic texture in Fe/Ir(111). Carefully analyzing STM images of the magnetic texture, we identify a uniaxial incommensurability and the crystallographic orientation along which the phason mode is expected to be sliding the texture. This is explicitly verified by atomistic spin simulations on a large unit cell that corresponds to a commensurate approximation of the magnetic order. These theoretical expectations are confirmed experimentally with our STM setup. The phason mode can be excited with the STM tip leading to random telegraph noise in the tunneling current, that we ascribe to the presence of two metastable minima in the phason potential due to the presence of disorder in our sample.

Results

Uniaxial incommensurability of the magnetic texture in Fe/Ir(111)

Figure 1b presents an atomically resolved STM topography of a single monolayer of Fe on Ir(111) recorded with a spin-polarized tip. The well-known magnetic texture of non-collinear spins¹³ can clearly be seen in the topography as an approximate square lattice. The corresponding Fourier-transformed image shown in Fig. 1c gives information on the magnetic unit cell with respect to the atomic crystal structure. The green circles represent

atomic lattice spots that are well approximated by a hexagonal lattice. Its primitive reciprocal lattice vectors are shown by the green arrows \mathbf{g}_1 and \mathbf{g}_2 . The blue and yellow circles mark magnetic spots due to the tunneling magnetoresistance (TMR) and tunneling anisotropic magnetoresistance (TAMR), respectively¹⁵. The blue circles correspond to lowest order magnetic Bragg peaks with primitive vectors \mathbf{G}_1 and \mathbf{G}_2 , whereas the yellow circles are higher-order peaks located at $\pm \mathbf{G}_1 \pm \mathbf{G}_2$ and $\pm \mathbf{G}_1 \mp \mathbf{G}_2$ around each atomic Bragg peak. The angle enclosed by the primitive vectors differs from 90°, indicating that the magnetic periodicity is clearly distinct from a square lattice. There exists, however, a commensurability between the magnetic and the atomic periodicities given by the relation $\mathbf{g}_1 + \mathbf{g}_2 = 3(\mathbf{G}_1 + \mathbf{G}_2)$.

The corresponding lattices in real space are shown in Fig. 1a with \mathbf{a}_i and \mathbf{A}_i being primitive vectors of the atomic and magnetic lattice, respectively, with the standard relations $\mathbf{a}_i \cdot \mathbf{g}_j = 2\pi\delta_{ij}$ and $\mathbf{A}_i \cdot \mathbf{G}_j = 2\pi\delta_{ij}$ where $i = 1, 2$. We find $|\mathbf{A}_1| = |\mathbf{A}_2| \approx 3.37a \approx 9.15 \text{ \AA}$, and $\angle(\mathbf{A}_1, \mathbf{A}_2) \approx 79.2^\circ$. The combinations $\mathbf{a}_\pm = \mathbf{a}_1 \pm \mathbf{a}_2$ are the primitive vectors of the equivalent centered rectangular lattice of the Fe monolayer. The vectors $\mathbf{a}_{+/-}$ define two important orthogonal directions that we denote in the following as *hard* and *soft*, respectively. The 3-fold commensurability is obtained along the hard direction $\mathbf{A}_1 + \mathbf{A}_2 = 3\mathbf{a}_+$. Along the soft direction \mathbf{a}_- , the magnetic texture appears to be incommensurate with the atomic crystal. These findings are completely consistent with the previous report of Heinze et al.¹³. The orange lines in Fig. 1a indicate the 3 × 5 commensurate approximation of the magnetic unit cell that possesses a 5-fold commensurability along \mathbf{a}_- . Note that this commensurate unit cell is also distinct from a square, because its smaller vertex angle is approximately 87.8° and thus smaller than 90°.

Theoretical prediction of a magnetic phason mode

The uniaxial incommensurability identified above implies the existence of a gapless phason mode describing the sliding of the magnetic order along the soft \mathbf{a}_- direction, which follows for infinitely large, clean systems from very general arguments¹. Nevertheless, in order to investigate theoretically the emergence of the phason mode, we performed atomistic spin simulations of the extended Heisenberg model put forward by Heinze et al.¹³, that reproduces important features of the observed magnetic texture in Fe/Ir(111). It consists of Heisenberg, Dzyaloshinskii-Moriya, biquadratic, and four-spin exchange interactions as well as uniaxial anisotropy, see “Methods” for

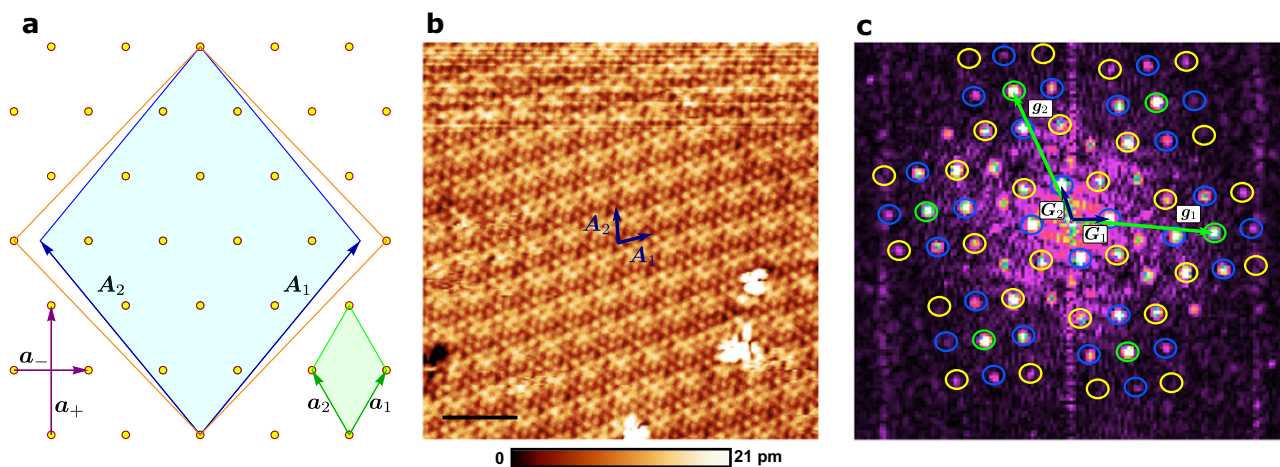


Fig. 1 | Atomic and magnetic structure of Fe/Ir(111). **a** Atomic and magnetic Bravais lattices of Fe/Ir(111). Yellow dots represent the hexagonal lattice of Fe atoms, with a unit cell given by the green-shaded rhombus and primitive vectors \mathbf{a}_1 and \mathbf{a}_2 , with $\mathbf{a}_\pm = \mathbf{a}_1 \pm \mathbf{a}_2$. The blue-shaded rhombus is a primitive unit cell of the magnetic order, with primitive vectors \mathbf{A}_1 and \mathbf{A}_2 . The magnetic order possesses a uniaxial commensurability, $\mathbf{A}_1 + \mathbf{A}_2 = 3\mathbf{a}_+$. The orange lines represent the 3 × 5 commensurate approximation of the magnetic unit cell. **b** Atomically resolved spin-polarized STM image of the magnetic order ($U = 10 \text{ mV}$, $I = 15 \text{ nA}$) on Fe/Ir(111). The primitive vectors of the magnetic order of panel (a) are also indicated. The

topographic color code is given in the legend. The scale bar is 2 nm. **c** Fourier transform of the image in (b). Green circles and green arrows denote reciprocal lattice spots of Fe atoms and primitive vectors, respectively. Blue circles and blue arrows denote magnetic reciprocal lattice spots and primitive vectors, respectively, obtained via the TMR effect. Yellow circles are obtained via TAMR and correspond to higher-order magnetic Bragg peaks. The magnetic order possesses the commensurability $\mathbf{g}_1 + \mathbf{g}_2 = 3(\mathbf{G}_1 + \mathbf{G}_2)$. The corresponding lattices in real space are shown in panel (a).

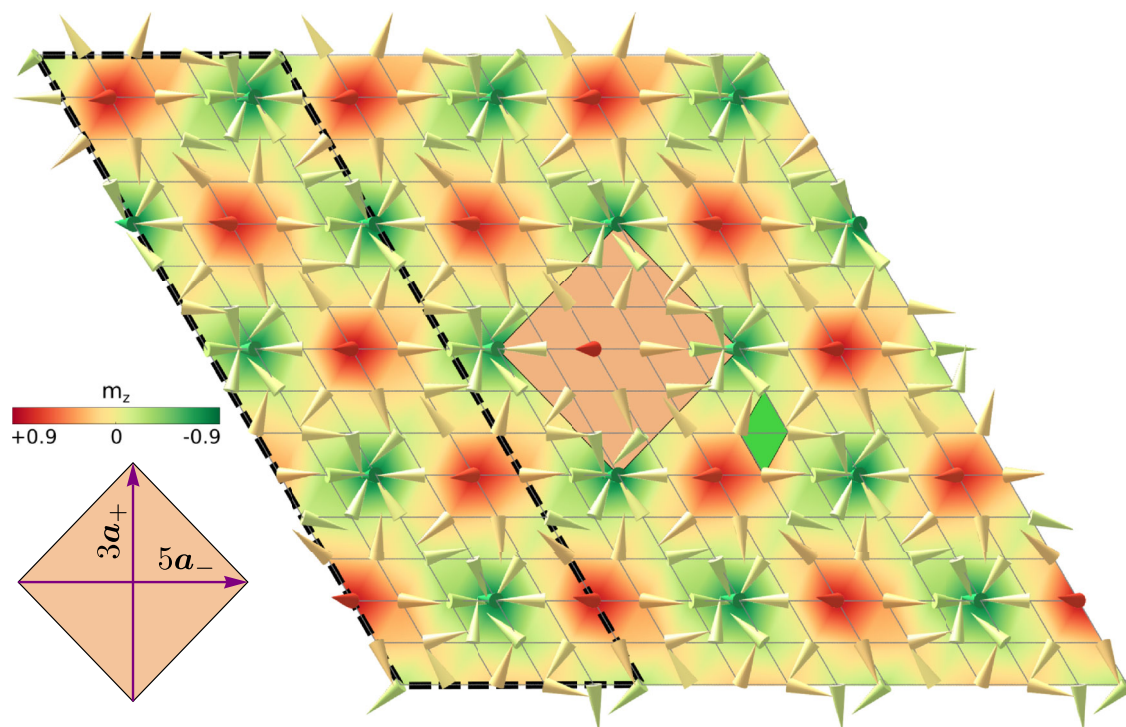


Fig. 2 | Atomistic spin simulation of the 3 × 5 commensurate magnetic texture. The green- and orange-shaded regions indicate the atomic unit cell and the commensurate approximation of the magnetic unit cell, cf. Fig. 1a. The region marked by a dashed line is the smallest common unit cell of the system. The supercell chosen for

the simulation is three times larger and contains 15 × 15 magnetic atoms. The unit cell on the left-hand side indicates the \mathbf{a}_\pm directions with the respective commensurabilities.

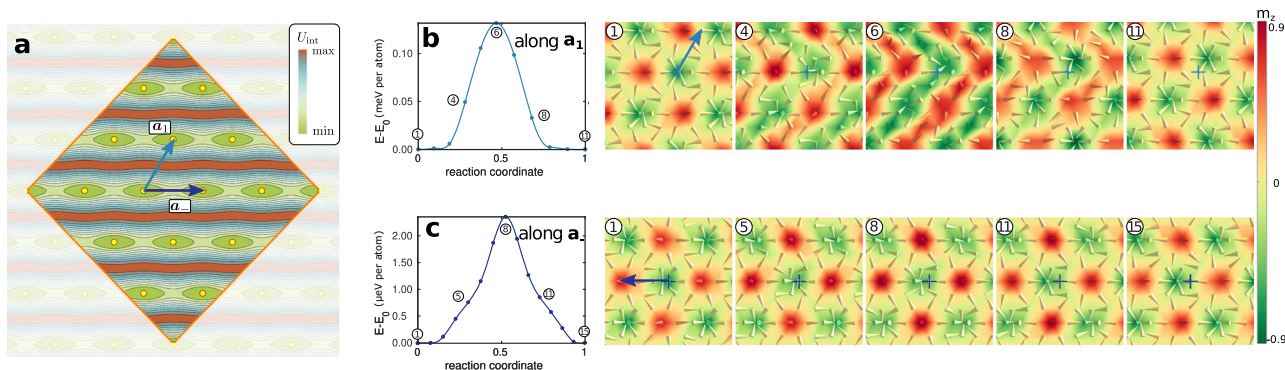


Fig. 3 | Geodesic nudged elastic band calculations. **a** Illustrative sketch of the effective potential for the sliding phason mode for the 3 × 5 commensurate magnetic texture of Fig. 2, see “Methods” for details. **b, c** Geodesic nudged elastic band calculations for a shift of the magnetic texture along the \mathbf{a}_+ and \mathbf{a}_- directions, respectively. The panels on the left- and right-hand side depict, respectively, the energy per

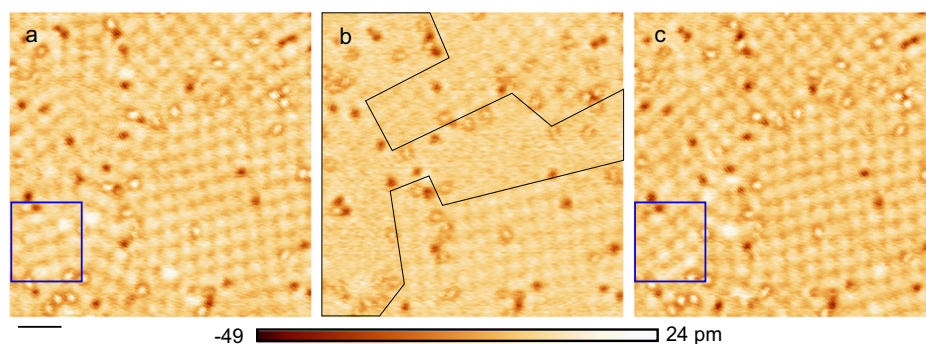
atom (blue dots and blue, interpolated curve) and magnetic configurations along the transition path. The cross markers on the left panels mark the initial position of an arbitrary spin initially pointing down. The energy barriers for the two cases differ by two orders of magnitude.

details. As an atomic simulation of an incommensurate magnetic texture is not feasible in a finite model, we limited ourselves to its 3 × 5 commensurate approximation, see orange lines in Fig. 1a. For that purpose, a supercell containing 15 × 15 magnetic moments positioned on the sites of the hexagonal atomic lattice was chosen; periodic boundary conditions were imposed that necessarily lead to the resulting ground state shown in Fig. 2 and reproduces the magnetic texture of ref. 13.

Generically, it is expected that the energetic cost for a shift of the magnetic texture increases with its commensurability, i.e., the potential barrier along the hard \mathbf{a}_+ direction should be larger than along the soft \mathbf{a}_- direction, see Fig. 3a. In order to confirm this expectation and to determine the effective potential for the phason mode, we performed geodesic nudged elastic band calculations, see “Methods” for details. In

particular, we considered a continuous shift of the texture along the two primitive vectors \mathbf{a}_+ and \mathbf{a}_- of the atomic lattice. We also checked that a shift along $\mathbf{a}_2 = \mathbf{a}_+ - \mathbf{a}_-$ yields the same results as the shift along \mathbf{a}_+ . During these calculations, the minimum energy path between the initial and final states is determined. The evolution of the energy is shown in Fig. 3b and c, together with examples of intermediate configurations of the magnetic texture. The explicit calculations show that the potential barrier for a shift along \mathbf{a}_+ is indeed about two orders of magnitude larger than along the soft \mathbf{a}_- direction. Moreover, the magnetic configuration is strongly deformed along the \mathbf{a}_+ path. This implies that a shift along the hard direction does not involve only the phason excitation, but rather a superposition of additional modes, whose characteristics have been discussed in detail in ref. 16. In contrast, the

Fig. 4 | STM induced changes of the magnetic texture. **a** Topographic STM image of the magnetic texture observed at bias voltage $U = 10$ mV and tunneling current $I = 10$ nA. The scale bar is 2 nm. **b** The same area scanned at an elevated bias voltage of $U = 100$ mV where the magnetic texture appears to be blurred within regions of the spin texture. These regions, as determined by eye, have been marked by black lines. **c** The subsequent image recorded at $U = 10$ mV shows again a static texture where minor modifications with respect to panel (a) can be spotted, e.g., in the area marked by the blue box. The legend indicates the color code of the topographic height.



intermediate configurations for the a_{\perp} path are basically undeformed during the shift and appear to be well captured by a single phason mode.

The simulations confirm that the sliding of the 3×5 commensurate magnetic texture along the soft a_{\perp} direction is well described by a phason that, however, possesses a small gap due to the five-fold commensurability in our calculations using a supercell. When a fully incommensurate structure is assumed in an infinite, defect-free sample, this small gap is expected to vanish. The magnetic texture realized in Fe/Ir(111) lacks this five-fold commensurability and is basically incommensurate along the soft direction, see Fig. 1, so that in the experimental system the phason is expected to show an even smaller barrier for sliding in realistic situations and the sliding mode may become gapless at least in the absence of disorder.

Experimental detection of the phason in Fe/Ir(111)

Figure 4a presents the magnetic texture on a larger scale recorded with STM topography at a bias voltage of $U = 10$ mV. The image contrast results from the TMR and TAMR effect¹⁵. Several different rotational domains can be identified, as well as local defects that give stronger contrasts.

When measuring at a higher bias voltage of $U = 100$ mV, see Fig. 4b, the spin texture becomes blurry or vanishes in some regions of the sample that are marked by black lines. This indicates that the magnetic texture in these regions is influenced by the action of the STM tip, i.e., it is either destroyed, melted or it is floating on the time scale of the STM experiment. Changing the voltage back to 10 mV subsequently reestablishes the static magnetic texture, see Fig. 4c, albeit not in the exact same order as previously. Some rearrangements of the domains or change of orientation can be observed, e.g., by comparing the texture in the area marked by the blue boxes in panels a and c. The magnetic textures can thus be manipulated by the STM tip, as has been already demonstrated previously by von Bergmann et al. using short voltage pulses^{15,17}. We found, however, that most of the magnetic domains remained static in our sample even when scanned at elevated voltages. This suggests that the manipulation threshold depends on the local disorder configuration.

A potential origin for the blurred images at larger bias voltage is the excitation of the phason mode of the magnetic texture induced by the STM tip. In order to test this hypothesis, we studied the dynamical behavior of the texture within this area in more detail. Figure 5a shows an STM scan of the investigated area where the white circle indicates a structural defect of the Fe film that is immobile and serves as a reference point. After placing the tip at the position of the white cross, the system was locally excited by increasing the bias voltage to $U = 80$ mV and, in addition, applying a micro-wave ac voltage with amplitude $U_{ac} = 27.2$ mV at 2 GHz between the tip and the sample. For the calibration of the ac voltage and the rectification of the dc current I_{NL} (see “Methods”). Under these conditions, the spin texture is excited only mildly so that the STM experiment with its limited bandwidth allows to detect individual changes in the spin texture. Figure 5b shows the time trace of I_{NL} that exhibits a random telegraph noise (RTN) with a two-level switching characteristics, i.e., the spin texture switches only between two states. In the initial state, I_{NL} is high and switches several times from high to low and back within the 15 s of the measurement. At the end of the

interval, I_{NL} is in the low-current state. Afterwards, an STM image of the final state was recorded and is presented in Fig. 5c. Comparing the relative positions of the contrast and the white cross, we observe that the magnetic texture between its initial and final state is shifted by ~ 0.25 nm along the incommensurate direction, which is close to the atomic nearest-neighbor distance, $a = 2.715$ Å, of fcc Fe on Ir(111)¹³, while the defect is not shifted. This rules out changes of the atomic configuration of the tip apex as a cause for the shift in the spin texture. Also note that the TAMR contrast is determined by the spin configuration of the sample. We exclusively found shifts of the spin texture along the incommensurate direction, switching back and forth between two states. As discussed above, shifts along the commensurate direction would require about two orders of magnitude more energy. Tunneling currents providing this much more energy are not feasible without field evaporation of the tip or sample and could thus not be applied. Moreover, inspection of the atomically resolved STM image in the inset of Fig. 5c reveals that the lateral shift is along the incommensurate, soft a_{\perp} crystallographic direction, see Fig. 1. Figure 5d, e shows a similar switching between two configurations on a differently oriented domain of the same sample linked by a translation by two atomic distances along the incommensurate direction.

The lateral shifts are thus explained with the excitation of the sliding phason mode of the texture. It appears that this mode switches many times during the time trace of Fig. 5b between two (meta-)stable states leading to a random telegraph noise. Note that the switching between the states occurs on the time scale of seconds, and it is thus extremely slow compared to the applied GHz frequency. The time scale of the transient between the two states, is, however, too fast to be detected in STM. This also holds for the example shown in Fig. 5d, e such that a possible transitional state shifted by only one atomic distance cannot be resolved. It is likely that the (meta-)stable states are generated by the presence of disorder, the various finite domains, as well as the concomitant domain walls present in the sample, which are clearly visible in Fig. 4. In a perfect and infinite sample, the incommensurability along one direction would theoretically lead to a vanishing phason energy and thus to the absence of visibility of the square pattern of the spin texture in experiments. In this respect, the finite size of the domains and domain walls to other domains stabilize the pattern.

Dependence of the switching rate

In order to address the mechanism of phason excitation and the time needed for the transition from one to the other state, we systematically measured the RTN on a fixed spot on a domain but varying the ac amplitude, dc voltage, current, and micro-wave frequency (see Fig. 6). Note that prior to all frequency dependency measurement, the STM tip was positioned on the non-magnetic Ir(111) surface and the STM micro-wave transfer function was calibrated using the method described elsewhere¹⁸. The micro-wave loss in the transmission line was then compensated at the output of the micro-wave generator such that the ac voltage at the tunneling junction is constant for every

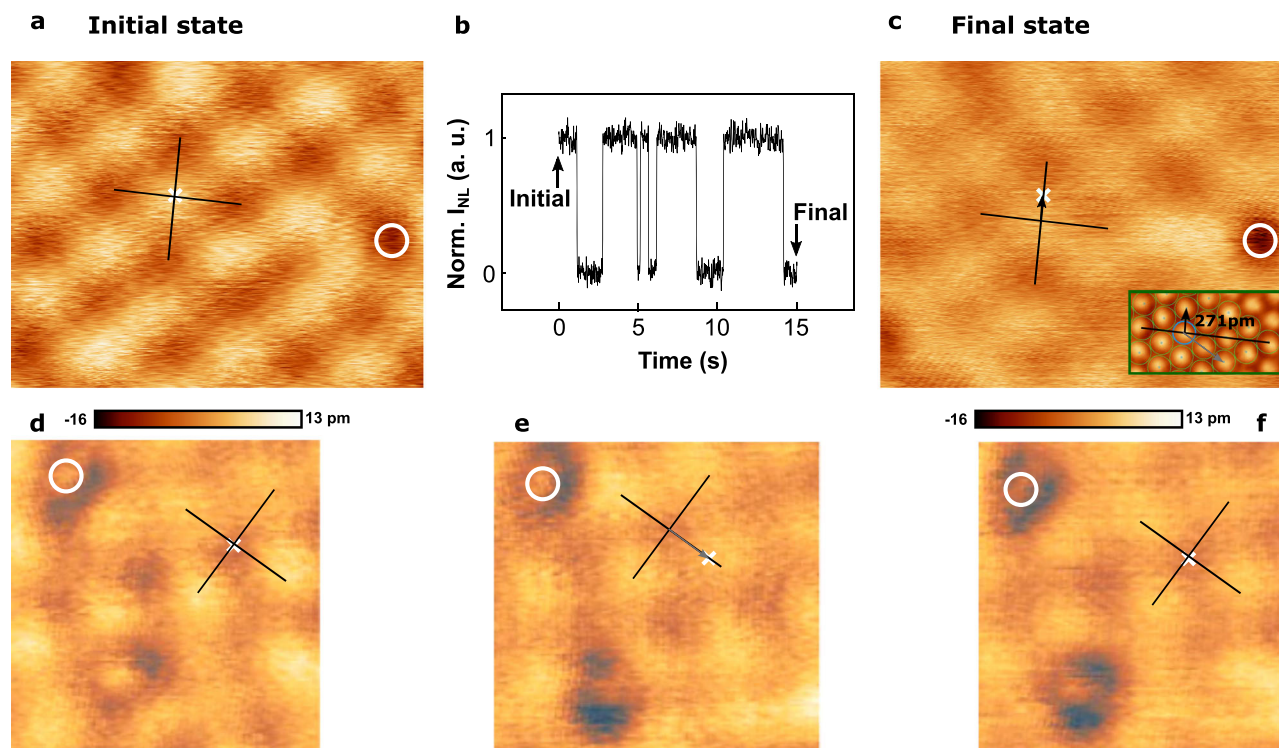


Fig. 5 | STM observation of the sliding phason. **a** STM image of the initial state where the white circle marks a defect that serves as a reference for the scan area ($U = 10$ mV, $I = 10$ nA). The time trace of panel (**b**) was recorded with the STM tip positioned at the location of the small white cross. The two black lines indicate the orientations \mathbf{a}_\pm of the crystallographic unit cell, see Fig. 1. **b** Time trace of the rectified current I_{NL} recorded at the position indicated by the white cross in (**a**) and (**c**) with $U = 80$ mV, $I = 20$ nA, and an additional ac voltage with amplitude $U_{ac} = 27.2$ mV at 2 GHz. **c** STM image of the final state ($U = 10$ mV, $I = 10$ nA). Compared to the initial

state, the magnetic texture is laterally displaced along the soft crystallographic \mathbf{a}_- direction. This is confirmed by the atomically resolved STM image of the crystal lattice shown in the inset with the indicated nearest-neighbor distance of the lattice. **d–f** Three STM images of switching events on the same sample but on a differently oriented domain illustrating a lateral displacement along the incommensurate direction by two atoms (gray arrow in the panels and the inset).

frequency. Clearly, the switching rate increases faster than linearly with both the ac amplitude and dc bias. Note that no ac voltage is necessary for switching, if the dc bias is high enough. The rate, however, scales linearly with tunneling current, indicating essentially a single-electron process. Interestingly, there is an asymmetry in the rates depending on the direction of the tunneling current. Always, a $\approx 30\%$ higher rate is observed for negative bias voltages, i.e., for tunneling of electrons from the tip into the sample. A simple heating mechanism leading to activated transitions would show a super-linear behavior with the electric power, i.e., it would steeply rise with both the sample bias and the tunneling current, which is not observed. Instead, the data suggests that the maximal voltage, i.e., the dc and ac components combined, needs to reach a threshold for the transitions, speaking for an inelastic tunneling mechanism, which also agrees with the linear current relation. As the tunneling current is spin-polarized due to the local magnetic order under the tip, there is a natural reason for an asymmetry of the rates, depending on the sign of the bias (and current) coming from excitations of magnetic structures via transfer of spin angular momentum between the tip and the sample. In the forward tunneling direction, minority electrons are required to inelastically excite the spin structure via magnon creation, while in the backward direction, majority electrons are needed such that the asymmetry reflects the spin-polarization of the tunneling current¹⁹. The observed asymmetry is in agreement with a switching mechanism via magnetic excitations with a minority spin-polarization of Fe. The frequency dependence is, however, rather weak, with a tendency of reduced switching rates above a micro-wave frequency of 3 GHz. As the data suggests, a critical value of the time-dependent bias voltage needs to be exceeded in order to induce a transition. The time, that the voltage exceeds this value, is only

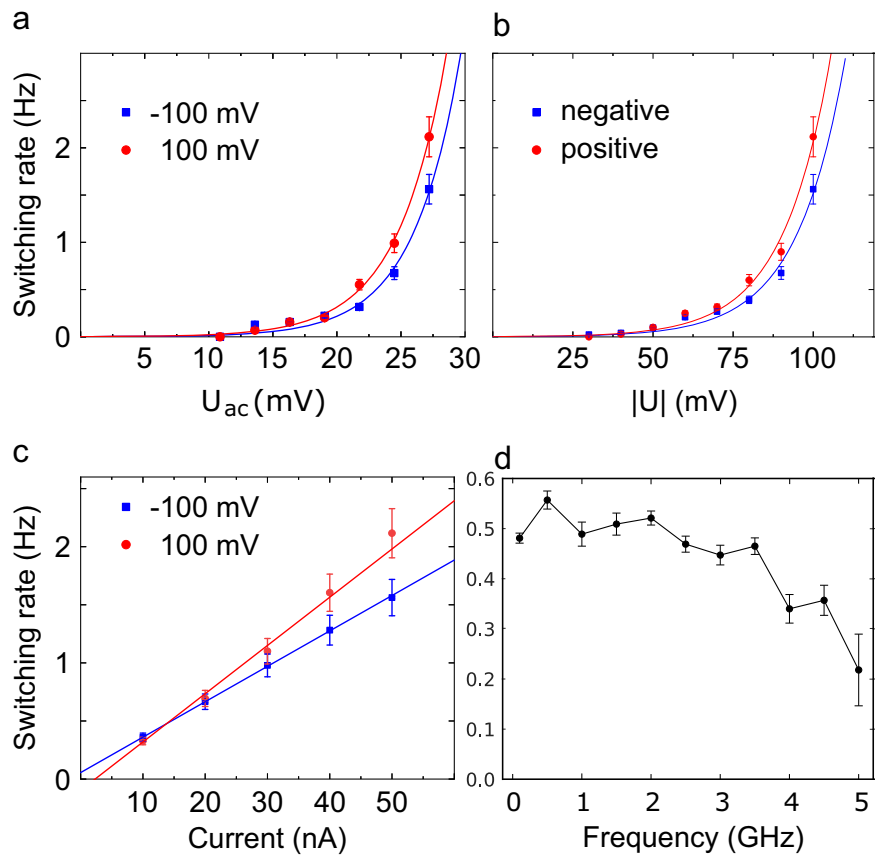
a fraction of the period of the ac frequency. Thus, the frequency dependence of the switching rate contains information about the time scale of the switching itself. Especially, when the duration of the voltage maximum exceeding the inelastic energy threshold for switching becomes shorter than the switching time, switching becomes less probable. In this case, the data suggests switching times of the order of 0.3 ns. Finally note that the threshold for the observation of the telegraph noise varies for different domains, as already indicated in the discussion of Fig. 4, highlighting the role of pinning of the spin texture by defects.

Discussion

In this work, we presented evidence for a low-energy magnetic excitation, i.e., a sliding phason mode of the uniaxially incommensurate magnetic texture of Fe/Ir(111). The activation of this mode was interpreted to be at the origin of blurred STM images of the magnetic texture shown in Fig. 4b. Further investigation on a specific magnetic domain revealed that the phason is pinned into two minima of an effective potential due to the presence of disorder in our sample. The STM tip was able to induce a switching between the two minima, leading to a random telegraph noise in the tunneling current with switching rates on the order of Hz.

This evidence for a sliding phason mode in the 2D magnetic Fe film raises interesting questions to be investigated in future research. In ideal samples with macroscopic domains without pinning by defects or boundaries, the phason is expected to be a gapless low-energy excitation. In a two-dimensional system, such a phason is able to destroy long-range magnetic order at finite temperature leading to a floating phase with the magnetic textures sliding along the incommensurate direction with liquid-like spatial correlations. Moreover, as a function of external parameters like

Fig. 6 | Dependency of the switching rate extracted from the telegraph noise on the external parameters. a Dependence on the ac amplitude, blue (red) squares data represent taken at -100 mV (100 mV). Solid lines are guides to the eye ($U = 100$ mV, $I = 50$ nA, 2 GHz excitation). **b** Dependence of the dc voltage (symbols as in (a), $I = 50$ nA, $U_{ac} = 27.2$ mV, 2 GHz excitation). **c** Dependence on the current. Solid lines show the linear fit of the data ($U = 100$ mV, $U_{ac} = 27.2$ mV, 2 GHz excitation). **d** Dependence on the micro-wave frequency ($U = 100$ mV, $I = 15$ nA, $U_{ac} = 27.2$ mV). The error bars represent the 1σ statistical error.



temperature or magnetic field, it might be possible to induce a commensurate-incommensurate transition where either the magnetic texture becomes fully incommensurate or fully commensurate with the atomic crystal lattice. Finally, the presence of a sliding phason mode should give rise to anisotropic responses to an applied spin current that will strongly depend on its orientation with respect to the uniaxial incommensurability.

Methods

Scanning tunneling microscopy (STM)

Measurements were conducted with a home-built low-temperature (4.2 K) ultra-high vacuum ($p \approx 1 \times 10^{-10}$ mbar) STM paired with a Nanonis controller. The Ir(111) single-crystal was prepared by cycles of annealing (~ 1200 K) in an oxygen environment ($p \approx 1 \times 10^{-7}$ mbar) and high-temperature flashing (~ 1700 K). The Fe film was deposited onto the clean Ir(111) surface using an electron-beam evaporator at slightly elevated temperature. STM tips were electrochemically etched from W wires and cleaned in situ by flashing (~ 2500 K). Spin-polarized tips were prepared by depositing Fe on the W tips followed by soft annealing. The ac modulation was generated by a Rohde & Schwarz SMB100A signal generator, mixed to the dc bias voltage by a Mini-circuits bias tee (ZX85-12G-S+) and sent to the STM tip. The ac voltage was modulated in amplitude (100%) at a frequency below the cutoff frequency of the STM current amplifier (typically at 3 kHz). The supplementary current (ΔI) induced by the ac modulation was detected with a lock-in amplifier by modulating the ac amplitude. It is the sum of 2 contributions: $\Delta I = I_{NL} + I_b$, where I_{NL} corresponds to a rectification effect of the non-linear $I(U)$ characteristic when introducing micro-waves to the tunneling junction^{18,20,21}. The second term, I_b , corresponds to the spin rectification effect^{22–24}.

Atomistic spin simulations

We simulate a supercell comprised of 15×15 normalized magnetic moments \hat{m}_i on a hexagonal crystal lattice, with periodic boundary

conditions. Simulations are carried out with Matjes²⁵ and Spirit²⁶ atomistic frameworks, and the results are cross-checked between the implementations. We use the extended Heisenberg model Hamiltonian for Fe/Ir(111) from ref. 13 with parameters extracted from first-principles density functional theory (DFT) calculations,

$$\mathcal{H} = - \sum_{ij} J_{ij} (\hat{m}_i \cdot \hat{m}_j) - \sum_{ij} \mathbf{D}_{ij} \cdot (\hat{m}_i \times \hat{m}_j) - K \sum_i m_{z,i}^2 + \mathcal{H}^{\text{HOI}}, \quad (1)$$

where J_{ij} and D_{ij} are, respectively, the Heisenberg exchange and Dzyaloshinskii-Moryia interaction coupling constants, and K is the perpendicular magnetic anisotropy constant. \mathcal{H}^{HOI} contains higher-order interactions (HOI) of the form,

$$\mathcal{H}^{\text{HOI}} = - \sum_{ij} B_{ij} (\hat{m}_i \cdot \hat{m}_j)^2 - \sum_{ijkl} Q_{ijkl} [(\hat{m}_i \cdot \hat{m}_j)(\hat{m}_k \cdot \hat{m}_l) + (\hat{m}_i \cdot \hat{m}_l)(\hat{m}_j \cdot \hat{m}_k) - (\hat{m}_i \cdot \hat{m}_k)(\hat{m}_j \cdot \hat{m}_l)], \quad (2)$$

in which B_{ij} and Q_{ijkl} denote the biquadratic, and four-spin interaction coupling constants.

The relaxed ground state shown in Fig. 2 has an energy of -9.97 meV per atom. with respect to the ferromagnetic state¹⁶, which is comparable to the value of -7 meV per atom given in ref. 13 for the DFT unit cell.

Minimum energy paths for the translation of the magnetic texture along the different axes discussed in the main text are computed via the geodesic nudged elastic band (GNEB) scheme³⁷. The method minimizes the energy of magnetic configurations belonging to an effective elastic band within the multidimensional energy landscape by taking into account the curvature of configuration space. The energy minimization is carried out following negative gradient lines. The saddle point configuration at the top of the barrier is precisely relaxed with a climbing image scheme.

We find energy barriers $\Delta E_{a_{1,2}} = 0.13$ meV per atom for translation along $\mathbf{a}_{1,2}$, and $\Delta E_{a_-} = 2.7$ μ eV per atom for translation along \mathbf{a}_- , i.e., the soft direction.

Effective phason potential for a 3×5 commensurate magnetic texture

We elaborate on the construction of the effective phason potential expected for a 3×5 commensurate magnetic texture that is sketched in Fig. 3a. As discussed in the context of Fig. 1, the reciprocal lattice vectors of the magnetic lattice \mathbf{G}_i and the crystal lattice \mathbf{g}_i satisfy the relation $\mathbf{g}_1 + \mathbf{g}_2 = 3(\mathbf{G}_1 + \mathbf{G}_2)$. Only for the 3×5 commensurate approximation we have the additional relation $\mathbf{g}_1 - \mathbf{g}_2 = 5(\mathbf{G}_1 - \mathbf{G}_2)$, and thus solving for \mathbf{g}_i

$$\mathbf{g}_1 = 4\mathbf{G}_1 - \mathbf{G}_2, \quad \mathbf{g}_2 = -\mathbf{G}_1 + 4\mathbf{G}_2. \quad (3)$$

In general, it is expected that the size of the Fourier components of the phason potential decreases with decreasing commensurability. Restricting ourselves to the Fourier components with the most commensurate wavevectors, we approximated

$$U_{\text{int}}(\mathbf{r}) \approx -U_3 \cos((\mathbf{g}_1 + \mathbf{g}_2)\mathbf{r}) - U_4(\cos(\mathbf{g}_1\mathbf{r}) + \cos(\mathbf{g}_2\mathbf{r})) \quad (4)$$

where $U_{3/4} > 0$ and $U_4/U_3 \ll 1$ in the sketch of Fig. 3a. The phason potential obtained in the simulations, see in particular Fig. 3c, deviates from a single cosine which, in principle, can be accounted for by including higher-order Fourier components.

Data availability

The experimental data of this study are available from the corresponding author on reasonable request.

Code availability

The codes used in this study are available from the corresponding author on reasonable request.

Received: 12 March 2024; Accepted: 27 June 2024;

Published online: 11 July 2024

References

- Chaikin, P. M. & Lubensky, T. C. *Principles of Condensed Matter Physics* (Cambridge University Press, 1995).
- Lyuksyutov, I., Naumovets, A. G. & Pokrovsky, V. *Two-Dimensional Crystals* (Academic Press, Inc., 1992).
- Grüner, G. *Density Waves in Solids* (CRC Press, 1994).
- Van Smaalen, S. Incommensurate crystal structures. *Crystallogr. Rev.* **4**, 79–202 (1995).
- Overhauser, A. W. Observability of charge-density waves by neutron diffraction. *Phys. Rev. B* **3**, 3173–3182 (1971).
- Bak, P. & von Boehm, J. Ising model with solitons, phasons, and “the devil’s staircase”. *Phys. Rev. B* **21**, 5297–5308 (1980).
- Grüner, G. The dynamics of charge-density waves. *Rev. Mod. Phys.* **60**, 1129–1181 (1988).
- Brown, P. et al. Strong coupling superconductivity in a quasiperiodic host-guest structure. *Sci. Adv.* **4**, eaao4793 (2018).
- Ochoa, H. & Fernandes, R. M. Degradation of phonons in disordered moiré superlattices. *Phys. Rev. Lett.* **128**, 065901 (2022).

- Bruce, A. D. & Cowley, R. A. The theory of structurally incommensurate systems. *J. Phys. C: Solid State Phys.* **11**, 3609–3630 (1978).
- Dzyaloshinsky, I. Theory of helicoidal structures in antiferromagnets. *Soviet Phys. JETP* **20**, 665–668 (1965).
- von Bergmann, K. et al. Observation of a complex nanoscale magnetic structure in a hexagonal Fe monolayer. *Phys. Rev. Lett.* **96**, 167203 (2006).
- Heinze, S. et al. Spontaneous atomic-scale magnetic skyrmion lattice in two dimensions. *Nat. Phys.* **7**, 713–718 (2011).
- Meichel, T., Suzanne, J. & Gay, J.-M. 2-dimensional phases adsorbed on a square symmetry substrate - methane and argon on single-crystal MgO (100). *C. R. Acad. Sci. Paris* **303**, 989 (1986).
- Von Bergmann, K. et al. Tunneling anisotropic magnetoresistance on the atomic scale. *Phys. Rev. B* **86**, 134422 (2012).
- Desplat, L. & Dupé, B. Eigenmodes of magnetic skyrmion lattices. *Phys. Rev. B* **107**, 144415 (2023).
- Von Bergmann, K., Kubetzka, A., Pietzsch, O. & Wiesendanger, R. Interface-induced chiral domain walls, spin spirals and skyrmions revealed by spin-polarized scanning tunneling microscopy. *J. Phys. Condens. Matter.* **26**, 394002 (2014).
- Hervé, M., Peter, M. & Wulfhekel, W. High frequency transmission to a junction of a scanning tunneling microscope. *Appl. Phys. Lett.* **107**, 093101 (2015).
- Balashov, T. et al. Inelastic electron-magnon interaction and spin transfer torque. *Phys. Rev. B* **78**, 174404 (2008).
- Nunes Jr, G. & Freeman, M. R. Picosecond resolution in scanning tunneling microscopy. *Science* **262**, 1029–1032 (1993).
- Moult, I., Herve, M. & Pennec, Y. Ultrafast spectroscopy with a scanning tunneling microscope. *Appl. Phys. Lett.* **98**, 233103 (2011).
- Tulapurkar, A. A. et al. Spin-torque diode effect in magnetic tunnel junctions. *Nature* **438**, 339–342 (2005).
- Hervé, M., Peter, M., Balashov, T. & Wulfhekel, W. Towards laterally resolved ferromagnetic resonance with spin-polarized scanning tunneling microscopy. *Nanomaterials* **9**, 827 (2019).
- Baumann, S. et al. Electron paramagnetic resonance of individual atoms on a surface. *Science* **350**, 417–420 (2015).
- Buhl, P. M., Desplat, L., Boettcher, M., Meyer, S. & Dupe, B. Matjes (Version 1.1.0) [Computer software]. <https://doi.org/10.5281/zenodo.12685461> (2024).
- Müller, G. P. et al. Spirit: multifunctional framework for atomistic spin simulations. *Phys. Rev. B* **99**, 224414 (2019).
- Bessarab, P. F., Uzdin, V. M. & Jonsson, H. Method for finding mechanism and activation energy of magnetic transitions, applied to skyrmion and antivortex annihilation. *Comput. Phys. Commun.* **196**, 335–347 (2015).

Acknowledgements

B.D. and L.D. thank Sebastian Meyer, Joo-Von Kim for useful discussions, and Markus Hoffmann and Gideon Müller for their help with Spirit. H.H.Y. acknowledges funding by the Alexander-von-Humboldt Foundation. W.W. acknowledges funding by Deutsche Forschungsgemeinschaft (DFG) with grant Wu 394/15-1 and through CRC TRR 288 - 422213477 “ElastoQMat,” project B06. L.D. acknowledges funding by the University of Liège under Special Funds for Research, IPD-STEMA Programme. M.G. acknowledges funding by the DFG through CRC TRR 288 - 422213477 (project A11) and through SPP 2137 (project 403030645).

Author contributions

L.D., V.P.K. M.G. and B.D. carried out theoretical calculations and modeling. H.H.Y., M.H., and W.W. performed the STM experiments. H.H.Y., M.H., T.B., S.G., and W.W. analyzed the experimental data. H.H.Y., L.D., V.P.K., M.H., S.G., M.G., B.D., and W.W. prepared the figures. H.H.Y., L.D., V.P.K., M.G., B.D., and W.W. wrote the manuscript. All authors contributed to the final manuscript.

Funding

Open Access funding enabled and organized by Projekt DEAL.

Competing interests

The authors declare no competing interests.

Additional information

Correspondence and requests for materials should be addressed to Wulf Wulfhekel.

Reprints and permissions information is available at <http://www.nature.com/reprints>

Publisher's note Springer Nature remains neutral with regard to jurisdictional claims in published maps and institutional affiliations.

Open Access This article is licensed under a Creative Commons Attribution 4.0 International License, which permits use, sharing, adaptation, distribution and reproduction in any medium or format, as long as you give appropriate credit to the original author(s) and the source, provide a link to the Creative Commons licence, and indicate if changes were made. The images or other third party material in this article are included in the article's Creative Commons licence, unless indicated otherwise in a credit line to the material. If material is not included in the article's Creative Commons licence and your intended use is not permitted by statutory regulation or exceeds the permitted use, you will need to obtain permission directly from the copyright holder. To view a copy of this licence, visit <http://creativecommons.org/licenses/by/4.0/>.

© The Author(s) 2024